12th International Conference on Fracture Mechanics of Concrete and Concrete Structures
FraMCoS-12
B.L.A. Pichler, Ch. Hellmich, P. Preinstorfer (Eds)

https://doi.org/10.21012/FC12.1275
MS11:5

# POROMECHANICAL APPROACH FOR PREDICTION OF FIRE-INDUCED FRACTURE AND MOISTURE TRANSPORT OF STRUCTURAL CONCRETE

**KEITAI IWAMA[*] AND KOICHI MAEKAWA[*]**

[*] Institute for Multidisciplinary Sciences, Yokohama National University
79-5, Tokiwadai, Hodogaya, Yokohama, Japan
e-mail: iwama-keitai-ft@ynu.ac.jp
maekawa-koichi-tn@ynu.ac.jp

**Key words:** Poromechanics, Crack, Spalling, Vapour pressure, Post-fire performance

**Abstract:** This study introduces a novel poromechanical approach to analyse fire-induced fractures and transport phenomena, such as spalling, crack propagation, and vapour pressure, by accounting for gaseous kinetics. A key feature of this framework is that, across all temperature ranges, vapour diffusion and the bulk movement of vapour and liquid water maintain thermodynamic equilibrium, while being coupled with the structural response of concrete. The increase in vapour pressure with rising temperatures, the non-orthogonal fractures of concrete (cracks and spalling) caused by vapour pressure and thermal stress, and the subsequent reduction in vapour pressure were confirmed. Notably, the proper release of vapour pressure after concrete cracking helped to prevent excessive damage. Focusing on the safety assessment of concrete structures, the study also investigated the post-fire performance of a reinforced concrete (RC) shear wall in a nuclear power plant. The proposed model effectively evaluated crack occurrence due to temperature increases, accelerated liquid water and vapour transport, the decrease in vapour pressure from crack propagation, and rapid liquid water penetration during post-fire-curing. The remaining capacity of the shear wall after 400°C heating was 95%, closely matching experimental results.

## 1 INTRODUCTION

The structural safety and durability of reinforced concrete (RC) are intricately linked to chemo-physical and mechanistic processes occurring within microscopic spaces, such as pores, which are thermodynamically equilibrated with their surrounding environment. Simultaneously, these chemo-physical processes are significantly influenced by macroscopic structural damages and deformations, such as cracking, which serve as rapid pathways for substances like vapour, water, and carbon dioxide.

To address these challenges in infrastructure design, maintenance, and safety assessment, it is essential to integrate structural kinetics and material mechanics. For instance, predicting fire-induced fracture behaviour and evaluating post-fire performance are critical for ensuring the long-term safety of concrete structures. In particular, explosive spalling during fire events poses severe threats to structural integrity. Fire-induced fractures and transport phenomena, including spalling, crack propagation, and vapour pressure buildup, involve complex interactions among thermodynamics, chemo-physics, fracture mechanics, and gaseous kinetics.

As a result, extensive efforts have been devoted to both numerical [e.g., 1-6] and experimental [e.g., 7-11] studies aimed at predicting explosive spalling [1-3,6-8,11] and assessing post-fire performance [4,5,9,10,12]. The authors have also sought to extend the

applicability of existing multi-scale modelling [13,14] up to 1,000°C, incorporating interactions with $CO_2$ (carbonation) [e.g., 15-17], as illustrated in Figure 1. This approach has demonstrated the ability to approximately capture the behaviour of RC members during and after exposure to high temperatures [e.g., 15,18].

This study introduces a novel poromechanical approach (see Figure 1G and

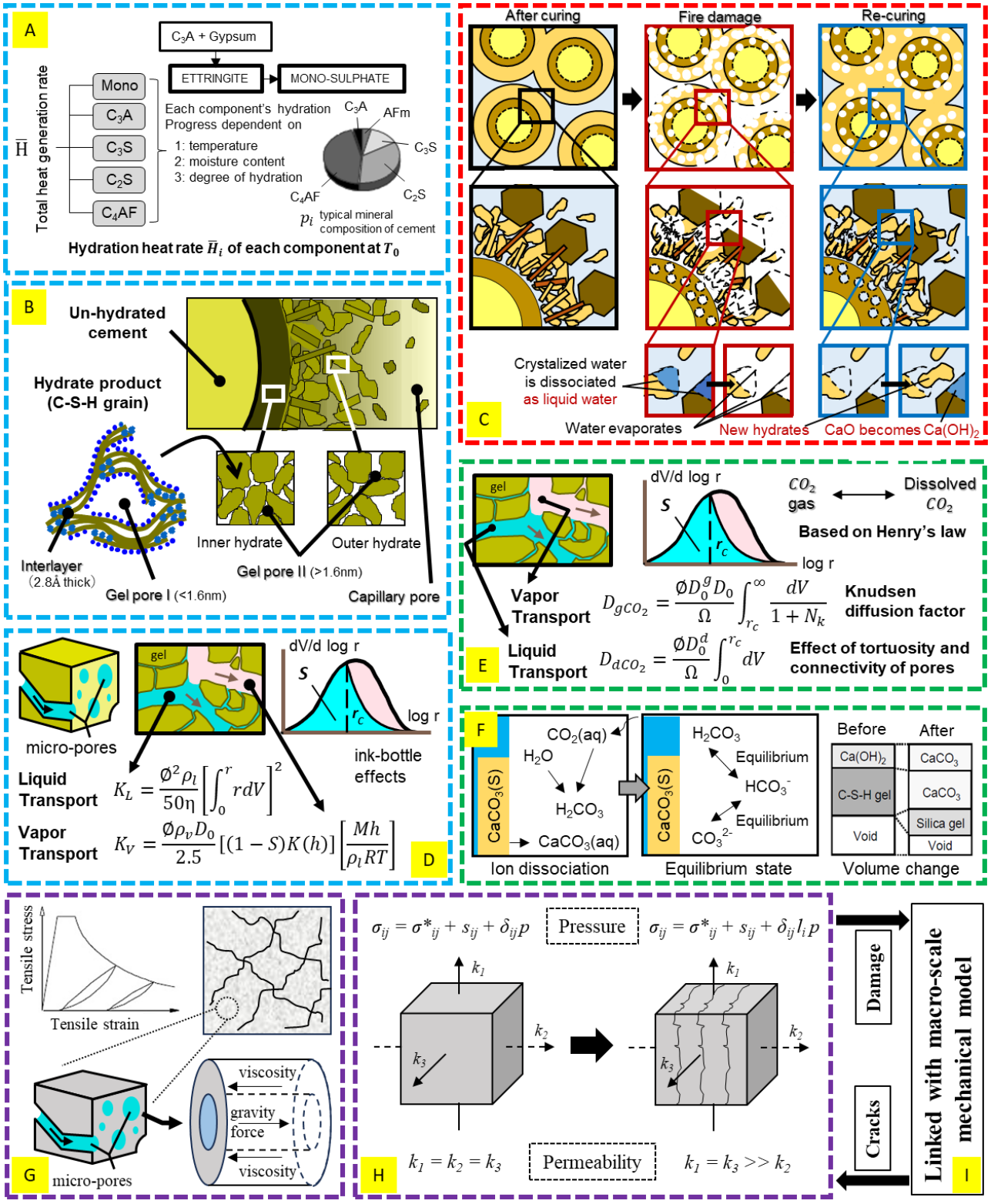


**Figure 1:** Outline of multi-scale modelling of structural concrete with poromechanical approach.

1H) to analyse fire-induced fractures and transport phenomena, such as spalling, crack propagation, and vapour pressure, by integrating gaseous kinetics. A comprehensive framework was proposed and verified to examine fracture and moisture transport mechanisms in structural concrete exposed to elevated temperatures. Furthermore, focusing on the safety assessment of concrete structures, this study investigated the post-fire performance of a cylindrical RC wall in a nuclear power plant.

## 2 MULTI-SCALE POROMECHANICAL SIMULATION PLATFORM

### 2.1 Brief overview of multi-scale platform

Figure 1 provides a concise overview of the multi-scale platform [13,14], including the upgraded model [15-18] for high-temperature environments. First, the degree of hydration for each chemical component in cement is determined using the multi-component hydration model based on the given mix proportions and environmental conditions (Figure 1A). This degree of hydration governs the gradual formation of the micro-pore structure in hardened cement paste (Figure 1B). The crystallized water of cement hydrates is released under high temperature environment, and the decomposed hydrates regain crystallized water under post-fire-curing in room temperature (Figure 1C). Using the micro-structure development model, the micro-pore structure is analysed to determine moisture transport and equilibrium based on pore structure and porosity (Figure 1D and 1E). Concurrently, mass transfer of $CO_2$ and other substances is accounted for, considering the porosity and saturation of the micro-pore structure (Figure 1F). Concrete skeleton deformation is evaluated alongside mixed pore pressures. These pore pressures drive substances into capillary pores and entrained air at the micro scale, creating reciprocal interactions that influence overall pore pressures and matrix deformation (Figure 1G). At the local scale, the flow of liquids into pores and cracks is modelled, coupling different flow phases (Figure 1H). Finally, by integrating the multi-directional cracking model of concrete into these micro- and meso-scale models, the platform incorporates macro-scale ($10^0$m-$10^2$m) structural analysis of RC (Figure 1I).

### 2.2 Governing equation of motion for liquid water and vapour

The kinematics of multiphase systems, which have been widely and successfully applied in geotechnical and structural engineering as well as in the study of multiphase chemo-physics in composites [19], were adapted and validated in the analysis of gas-blast-induced dynamic fractures in concrete [20]. This study applies the same framework to describe the mechanism of explosive spalling under high-temperature conditions, as outlined below:

Kinetics of coupled system;

$$\sigma_{ij,j} = \rho(\ddot{u}_i - g_i) + \rho_f \ddot{w}_i \tag{1}$$

Kinetics of pore substance;

$$p_i = \rho_f(\ddot{u}_i - g_i) + \frac{\rho_f \ddot{w}_i}{n} + \frac{1}{k_i}\dot{w}_i \tag{2}$$

General effective stress;

$$\sigma_{ij} = \tilde{\sigma}_{ij}(\varepsilon_{kl}) + \delta_{ij} p \tag{3}$$

Kinetics of pore substance;

$$\begin{aligned} p &= K_f \frac{w_{i,i} + \varepsilon_{ii}}{n} \\ w_{i,i} &= \frac{\partial w_x}{\partial x} + \frac{\partial w_y}{\partial y} + \frac{\partial w_z}{\partial z} \\ \varepsilon_{ii} &= \varepsilon_{xx} + \varepsilon_{yy} + \varepsilon_{zz} \end{aligned} \tag{4}$$

where, $\sigma_{ij}$ and $\varepsilon_{kl}$ are total stress and total strain tensors, $u_i$ is the displacement of the solid skeleton, $g_i$ is the gravity acceleration, $w_i$ is the relative displacement of the particle of pore substance from the solid skeleton, $\rho$ is the density of the combined solid-pore, $\rho_f$ is the density of the incompressible pore substance as constant, $n$ is the porosity, $k_i$ is the permeability of pore driven by the pressure gradient, $\tilde{\sigma}_{ij}$ is the effective stress of the solid skeleton, $p$ is the iso-parametric pore pressure, $K_f$ is the elasto-volumetric stiffness of pore substances. The subscript "$i$" denotes the component of the $i$-th coordinate, while the second subscript "$j$" indicates differentiation with respect to the $j$-th coordinate. Here, as shown in Equation (4), Einstein summation

convention is applied for tensorial expression.

Equation (1) represents the motion of the combined solid-pore mass, while Equation (2) governs the kinetics of pore substances relative to the motion of the solid skeleton. Equation (3) describes the fully saturated state of the solid-pore system, expressed through the effective stress of the solid skeleton, derived from both the strains of the solid skeleton and the volumetric strain of the pore substances. Equation (4) assumes isotropic elasticity and a constant density for the pore substances.

The original framework proposed by Biot [19], as described above, can be extended to compressible fluid media with nonconstant density, which varies depending on pore pressure. To address this complexity, we account for the strong nonlinearity introduced by the variable density of gas and its condensation. This is critical because the pore substance exists as a liquid before phase transformation and expands significantly upon transitioning to vapour, resulting in substantial density changes. In this study, the equations of motion for solid-liquid-gas phases are generalized in terms of mass motion to achieve a stable and reliable solution, as detailed below:

$$\sigma_{ij,i} = \rho(\ddot{u}_i - g_i) + \rho_0 \ddot{W}_i \tag{5}$$

$$p_i = s \cdot \rho_0(\ddot{u}_i - g_i) + \frac{\rho_0 \ddot{W}_i}{n} + \frac{1}{k_i \cdot s}\dot{W}_i \tag{6}$$

$$s \equiv \rho_f / \rho_0$$

$$\rho_0 W_i = \rho_f w_i \tag{7}$$

where $W_i$ is not the particles' motion of pore substance of liquid-gas but its mass motion in $i$-th direction from the solid skeleton, and the pore volume where liquid-gas may stay is denoted by "$n$" as above, and $\rho_0$ is the density of the pore substance at the referential state. Since $\rho_f$ is not constant but variable in this case, this nonlinearity is included in the main factor of $W$ as indicated by Equation (7).

The permeability of pore substances, represented by $k_i$ in Equation (6), determines the movement of pressurized gas through connected voids and crack paths formed under tensile forces. At the same time, gas permeation reciprocally influences the cracking process. These interdependent meso-scale phenomena can be incorporated into the solution process, which is a key advantage of the mass motion formulation. This approach also allows for the simultaneous resolution of these interacting events.

### 2.3 Crack and permeation for pore substances of liquid water and vapour

The thermodynamic phase equilibrium of the idealized gas is shown as

$$p_{vap} = P_{sat} exp\left(\frac{P_l M_w}{\rho_l RT}\right) \tag{8}$$

where $P_{sat}$ is the saturated vapour pressure, $P_l$ is the pore water pressure, $M_w$ and $\rho_l$ are the molar volume of liquid water and its density, $R$ is the gas constant, and $T$ is the absolute temperature. In this proposed model, the calculated vapour pressure is caused by vaporization accompanying volumetric expansion of water due to phase changes of crystallized water from cement hydrates as well as condensed free water. This capability is particularly important for ultra-high-strength concrete, which contains a significant amount of chemically bound water.

The total stress, including the effects of vapour pressure, is determined by solving the equilibrium between the solid and pore media while ensuring deformational compatibility and boundary conditions are satisfied. If the calculated tensile stress exceeds the material's tensile strength, cracks are assumed to form perpendicular to the principal stress direction, as depicted in Figure 1H.

Crack formation can create continuous pathways for the migration of pore substances. At the same time, pore substances reaching crack fronts can cause pressure increases, inducing additional tensile stresses that lead to further crack propagation. As a result, modelling the permeation of pore substances is essential. In this study, the kinetics of permeation, represented by $k_i$ in Equation (6), is formulated using the parallel plane flow model based on the Hagen-Poiseuille law.

Let $p_i$ denote the pressure gradient in the $i$-th coordinate direction, which drives the motion of the pore mass. For the basic equations governing gaseous flow through cracks,

laminate flow is assumed [21]. Figure 1H illustrates parallel crack planes, with the permeability of cracked concrete represented as a combination of the isotropic permeability of uncracked concrete and the permeability of cracks [21,22].

## 3. NUMERICAL SIMULATION FOR VAPOUR PRESSURE AND FRACTURE

### 3.1 Moisture transport at high temperature

The proposed model described in Chapter 2 was verified under a one-face heating condition, as illustrated in Figure 2. In the simulation, the temperature, free water content, and relative humidity of concrete with a water-cement ratio (W/C) of 50% were analysed during high-temperature exposure. Prior to heating, the concrete was sealed and cured at 20°C for 200 days. It was then subjected to one-face heating up to 1,000°C at a heating rate of 10°C/min (see Figure 2).

Figure 2 presents the simulation results, showing the depth distributions of temperature, free water content, and relative humidity within the micro-pores at 0, 10, 25, and 60 minutes from the start of heating.

The temperature distribution indicates a gradual increase in temperature over time, with a gradient developing from the heated surface inward. Regarding free water content, it is initially uniform throughout the depth of the concrete. However, as the temperature rises and the heated surface dries, the free water near the

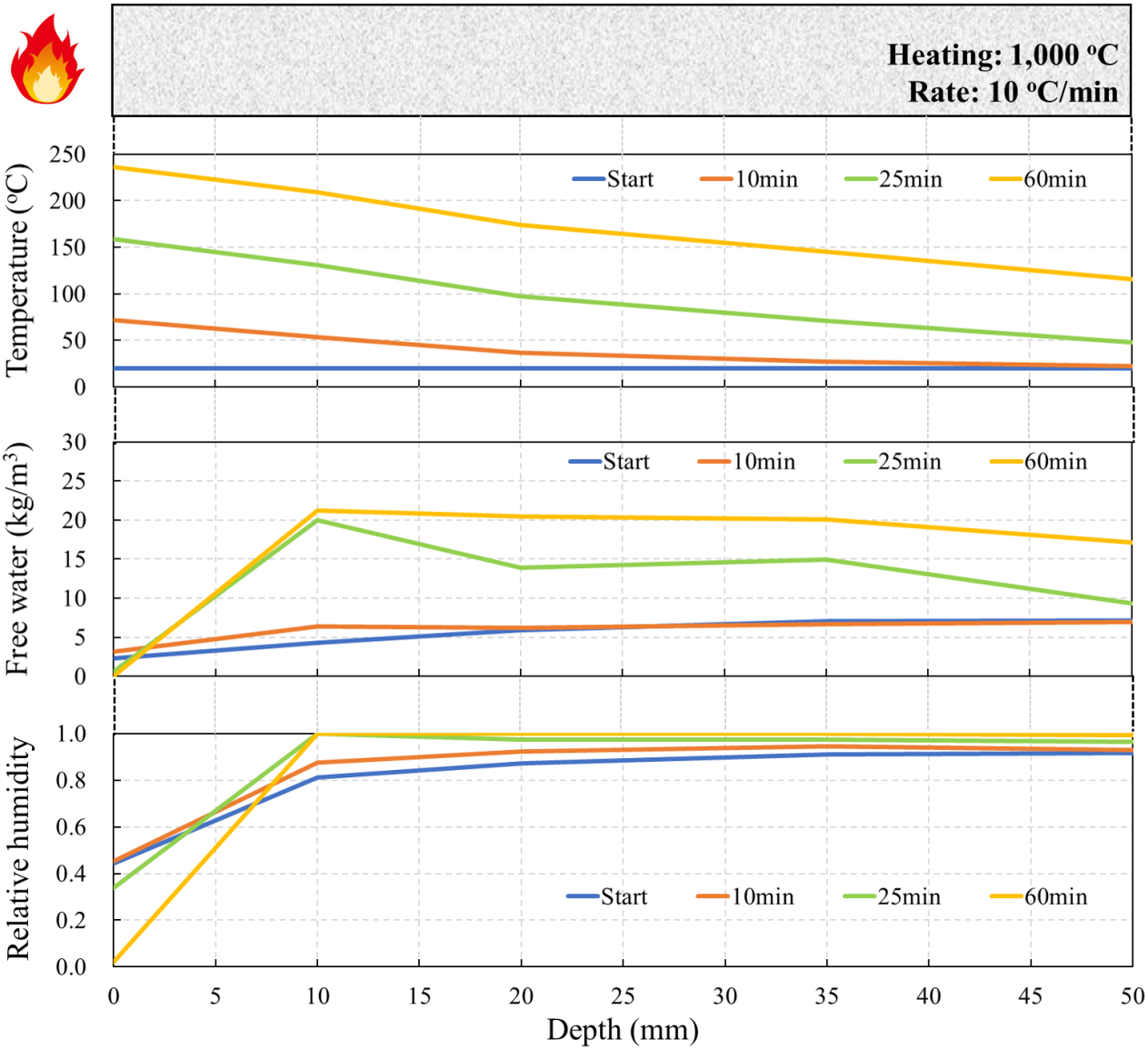


**Figure 2:** The depth distributions of temperature, free water content, and relative humidity.

surface decreases, while it accumulates further inside. This trend is further corroborated by the relative humidity distribution, which reveals a dry zone near the surface and a moist zone in the interior. These observations suggest that moisture migrates inward due to the temperature and pressure gradients, while crystallized water within the cement hydrates decomposes under high-temperature heating.

In conclusion, the proposed model demonstrates the ability to accurately predict moisture transport at high temperatures.

### 3.2 Fire-induced fracture and spalling

The proposed model was also validated for fire-induced fractures under one-face heating conditions, as depicted in Figure 3. The simulation, based on a previous study [23], involved three concrete mix proportions with W/C of 29%, 44%, and 62%. A thermal load was applied to one face of a prismatic sample (300 x 300 x 120 mm) using a radiant heater (see Figure 3). The average compressive strengths of the concrete with W/C ratios of 29%, 44%, and 62% at 28 days were 76 MPa, 53 MPa, and 35 MPa, respectively.

Figure 3 illustrates the principal strain distributions at 0, 50, 80, and 160 minutes after the onset of heating. These strain distributions highlight the fire-induced fractures (or damage) in the concrete.

At 50 minutes, damage due to stress concentration is observed near the four corners of the specimens, irrespective of concrete strength. At 80 minutes, in the high-strength concrete specimen (W/C of 29%), damage propagates laterally, with further deterioration in the centre of the specimen, suggesting

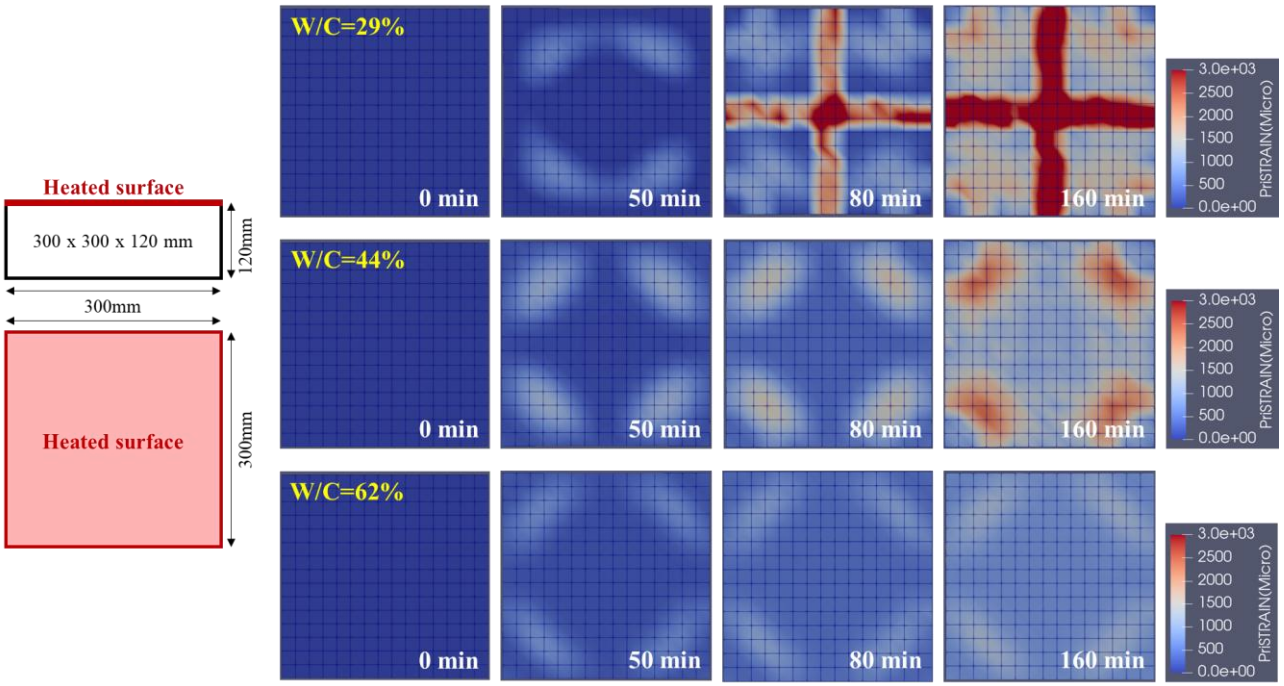


**Figure 3:** The fire-induced fractures illustrated by principal strain distributions.

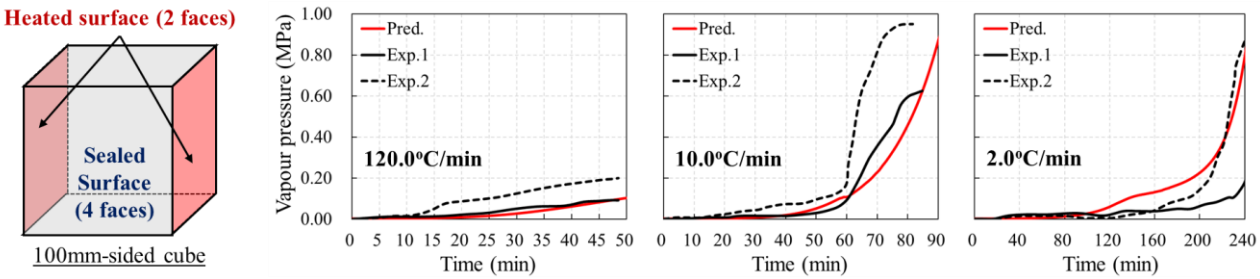


**Figure 4:** The distribution of vapour pressure at the centre of the specimens: compared to Felicetti *et al*. [24].

spalling and other forms of damage. At 160 minutes, the lateral damage in the high-strength concrete extends further, covering the entire heated surface. In contrast, for the normal-strength concrete specimens, the damage remains localized, primarily near the four corners, and is significantly less extensive than that in the high-strength specimen.

These findings align with existing knowledge that higher-strength concrete has a greater susceptibility to spalling and more extensive damage under fire exposure [e.g., 1-3,6,7]. This consistency further supports the validity of the proposed model.

### 3.3 Vapour pressure

The proposed model was further validated using experimental results from concrete specimens subjected to two-face heating, as illustrated in Figure 4. In the experiment [24], vapour pressure measurements were conducted on 100 mm concrete cubes exposed to two-face heating. The concrete mix had a W/C of 53.6%. After casting, the specimens were demoulded at 24 hours, sealed for 7 days, and subsequently cured in room conditions for 3 weeks. After this period, the specimens were sealed again and stored at room temperature until 90 days after casting. At the time of the heating test, the average compressive strength of the concrete was 37 MPa. At 90 days, the specimens were heated to 500°C, maintained at that temperature for 0.5 to 2 hours. Heating rates were set at 2.0, 10.0, and 120.0°C/min.

Figure 4 compares the simulation results with experimental data, showing the distribution of vapour pressure at the centre of the specimens during heating. Overall, the proposed model effectively predicts changes in vapour pressure within the concrete under high-temperature conditions, regardless of the heating rate.

For the heating rate of 120°C/min, both the experimental and simulation results show lower vapour pressure compared to the other cases. This is likely due to the rapid drying of the concrete surface caused by the large heating rate, coupled with thermal stress from the steep temperature gradient, which may have induced fine cracks. These cracks likely facilitated vapour release from the interior.

At heating rates of 10°C/min and 2°C/min, rapid increases in vapour pressure are observed after 60 minutes and 160 minutes, respectively. This is attributed to the concrete temperature reaching approximately 130°C, at which point both the liquid water in the pores and the water released from the decomposition of crystallized water of cement hydrates begin to vaporize.

As shown in Figure 4, discrepancies exist in the vapour pressure histories measured during the experiments, making it challenging to precisely predict the vapour pressure within concrete. However, the proposed model

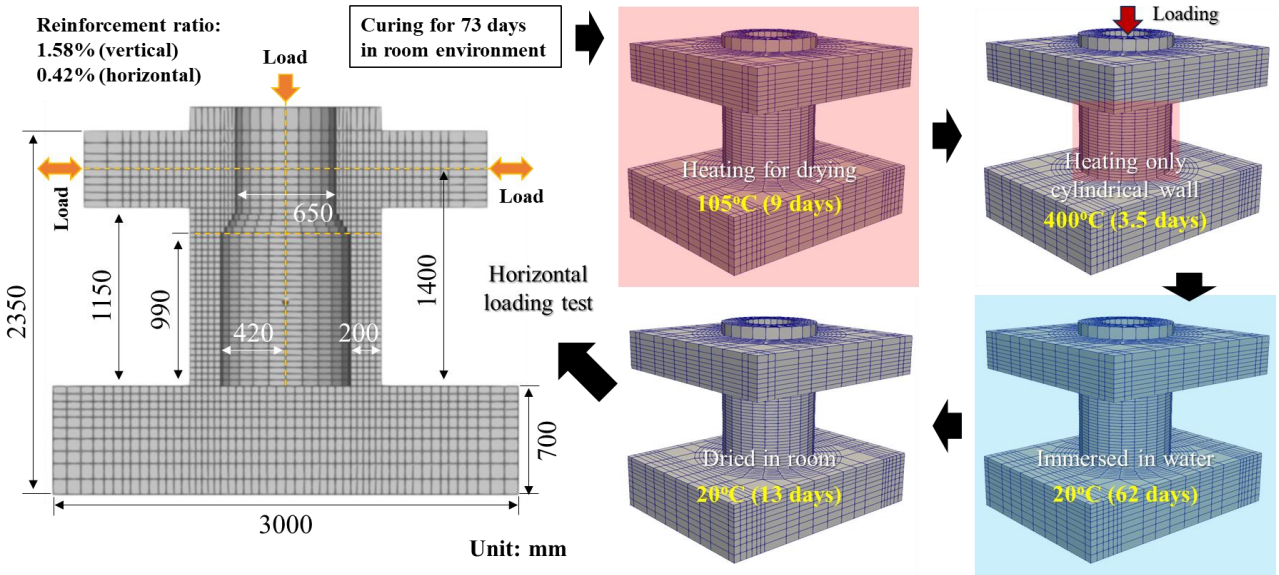


**Figure 5:** The numerical model and the procedure of the heating, post-fire-curing and loading [25].

successfully accounts for the transport of substances (liquid water and vapour) during heating, incorporating fire-induced fractures such as cracks, thereby demonstrating its validity.

## 4. NUMERICAL SIMULATION FOR POST-FIRE PERFORMANCE

The post-fire performance of infrastructure plays a critical role in enabling the rapid recovery and rational repair of structures subjected to fire damage. The authors aim to extend the application of the proposed model to include the post-fire-curing process, where damage induced by high-temperature exposure significantly influences mass transport under ambient conditions. As part of this effort, the study investigated a reinforced concrete (RC) structure utilized within nuclear power plants.

Globally, it is well-known that the Fukushima Daiichi Nuclear Power Plant (FD-NPP) experienced a catastrophic accident triggered by severe ground motion during the 2011 Great East Japan Earthquake. This event exposed the reactor pressure vessel (RPV) pedestal, a critical RC structure, to an extraordinarily high-temperature environment [25].

### 4.1 Simulation model

As illustrated in Figure 5, the structure under investigation is a cylindrical RC wall with a W/C of 55%, while the upper and lower stubs have a mix proportion of W/C of 40%. The experimental procedure is also detailed in Figure 5.

Initially, the specimen was cured under room conditions for 73 days. Following this, to facilitate drying, the entire specimen was placed in a furnace and heated to 105°C for 9 days. Subsequently, the cylindrical RC wall portion was subjected to a heating process, where the temperature was increased to 400°C at a rate of 1°C/min and maintained constant for 3.5 days. After natural cooling, the specimen underwent a two-phase post-fire-curing process; 62 days of immersion curing in water followed by 13 days of room curing.

Finally, the specimen was subjected to horizontal loading. The compressive strength of the cylindrical RC wall was 38 MPa before heating and decreased to 34.7 MPa after the post-fire-curing process.

### 4.2 Post-fire performance of cylindrical RC wall

Figure 6 illustrates the principal strain distribution of the cylindrical RC wall during the 3.5-day high-temperature heating phase. At the start of heating, the strain distribution reveals residual strain in the concrete due to the specimen's pre-heating history, having been dried for 9 days.

As the temperature increased, the strain within the cylindrical RC wall began to rise approximately 12 hours after heating commenced. This phenomenon is attributed to the evaporation of liquid water concentrated at

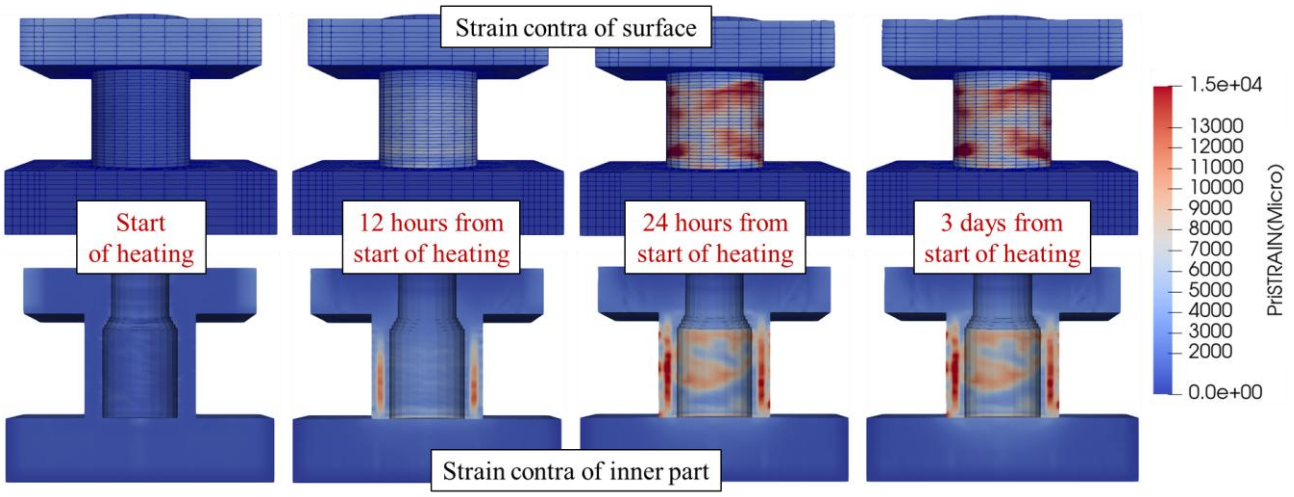


**Figure 6:** The principal strain distribution of the cylindrical RC wall during the 3.5-day heating.

the core of the wall, driven by the temperature and pressure gradients created by heating from both the inner and outer surfaces. After 24 hours, damage within the wall intensified, accompanied by significant surface damage. This damage is believed to result from vapour migration toward the wall's surface, where pressure is lower, under elevated vapour pressure, leaving behind cracks and other forms of damage. Once the wall's temperature stabilized and vapour was released, the strain distribution showed no substantial changes after three days of heating, indicating that the progression of damage had ceased.

Figure 7 depicts the relationship between horizontal load and deformation angle. Following the post-fire-curing phase detailed in Figure 5, the cylindrical RC wall was subjected to horizontal loading. Referring to the experimental study [25], the deformation angle was defined as the ratio of horizontal displacement to the wall height ($\delta/h$, see Figure 7).

Overall, the proposed model effectively predicts the post-fire performance of the cylindrical RC wall, encompassing aspects such as load capacity, stiffness, and deformation. Figure 7 also displays the strain distribution and deformation of the wall during horizontal loading. As the load increased, shear damage emerged within the wall, accompanied by concrete cracking, deformation caused by rebar pull-out in the tension zone, and compressive failure of concrete in the compression zone. These observations indicate that the model can replicate the behaviour of load reduction during repeated loading after reaching the peak load.

Finally, the simulation results indicate that the remaining load capacity of the heated cylindrical RC wall was 1567 kN, approximately 95% of the load capacity of the sound (unheated) wall, closely aligning with experimental findings. This demonstrates that when concrete is exposed to temperatures up to around 400°C, its residual performance remains nearly equivalent to that of unheated concrete, owing to the restoration of its strength through subsequent post-fire-curing.

## 5 CONCLUSIONS

This study proposed a numerical simulation platform utilizing a poromechanical approach to account for fire-induced fractures and moisture transport in concrete. The conclusions are summarized as follows:

1) The poromechanical approach successfully enabled the theoretical prediction of fire-induced damage during high-temperature heating and the subsequent transport of liquid water and vapour within the concrete.
2) The proposed model accurately quantified changes in vapour pressure inside the concrete during high-temperature exposure. This demonstrates the model's ability to appropriately calculate both the damage and mass transport processes occurring within the material.

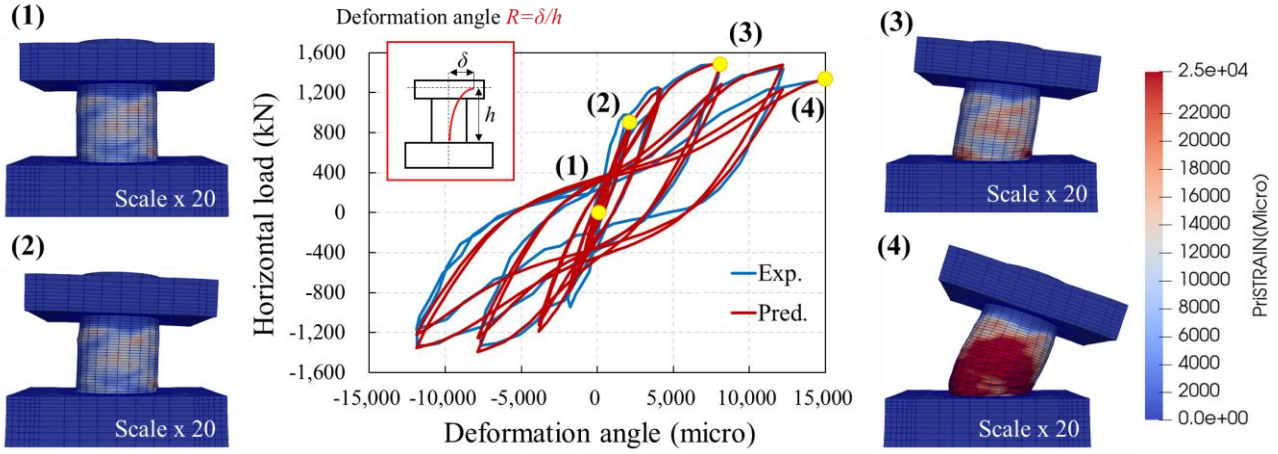


**Figure 7**: The relationship between horizontal load and deformation angle and the strain distribution and deformation of the cylindrical RC wall during horizontal loading.

3) Through an investigation of the post-fire performance of a cylindrical RC wall, the proposed model demonstrated its capacity to predict the residual structural performance with a high degree of accuracy. This confirms that the model effectively captures fire-induced damage and mass transport during high-temperature heating, as well as the transport phenomena and strength recovery of concrete during the cooling and post-fire-curing phases.

## REFFERENCES


[1] Gawin, D., Pesavento, F. and Schrefler, B.A., 2006. Towards prediction of the thermal spalling risk through a multi-phase porous media model of concrete, *Computer Methods in Applied Mechanics and Engineering*, Volume 195, Issue 41-43, 2006; pp.5707-5729.

[2] Zhang, H.L. and Davie, C.T., 2013. A numerical investigation of the influence of pore pressures and thermally induced stresses for spalling of concrete exposed to elevated temperatures. *Fire Safety Journal*, Volume 59, 2013; pp.102-110.

[3] Kodur, V. and Banerji, S., 2021. Modeling the fire-induced spalling in concrete structures incorporating hydro-thermo-mechanical stresses. *Cement and Concrete Composites*, Volume 117, 2021; Article ID: 103902.

[4] Wang, H., Lyu, H., Liu, T., Li, Y. and Tan, K.H., 2022. Effect of post-fire curing on compressive strength of ultra-high performance concrete and mortar, *Construction and Building Materials*, Volume 346, 2022; Article ID: 128447.

[5] Zhang, Y., Zhang, X., Zhang, R., Ni, W., Zhi, W. and Wang, L., 2024. Fire and post-fire performance of unbonded semi-precast prestressed reinforced concrete beams, *Engineering Structures*, Volume 308, 2024; Article ID: 117961.

[6] Hernández-Figueirido, D., Reig, L., Melchor-Eixea, A., Roig-Flores, M., Albero, V., Piquer, A. and Pitarch, A.M., 2024. Spalling phenomenon and fire resistance of ultrahigh-performance concrete, *Construction and Building Materials*, Volume 443, 2024; Article ID: 137695.

[7] Hertz, K.D., 2003. Limits of spalling of fire-exposed concrete, *Fire Safety Journal*, Volume 38, Issue 2, 2003; pp.103-116.

[8] Banerji, S., Kodur, V. and Solhmirzaei, R., 2020. Experimental behavior of ultra high performance fiber reinforced concrete beams under fire conditions, *Engineering Structures*, Volume 208, 2024; Article ID: 110316.

[9] Shachar, Y.M. and Dancygier, A.N., 2020. Assessment of reinforced concrete slabs post-fire performance, *Fire Safety Journal*, Volume 111, 2020; Article ID: 102932.

[10] Oğuz Akın Düzgün, Q.A. and Küçük, E.N., 2024. Post-fire seismic performance of reinforced concrete structures, *Structures*, Volume 59, 2024; Article ID: 105718.

[11] Jiang, J., Wu, M. and Ye, M., 2024. Prediction of fire spalling behaviour of fibre-reinforced concrete, *Magazine of Concrete Research*, Volume 76 Issue 5, 2024; pp.229-244.

[12] Li, L., Shi, L., Wang, Q., Liu, Y., Dong, J., Zhang, H. and Zhang, G., 2020. A review on the recovery of fire-damaged concrete with post-fire-curing, Construction and Building Materials, Volume 237, 2020; Article ID: 117564.

[13] Maekawa, K., Pimanmas, A., and Okamura, H., 2003. *Nonlinear Mechanics of Reinforced Concrete*, Spon Press.

[14] Maekawa, K., Ishida, T., and Kishi, T., 2008. *Multiscale Modeling of Structural Concrete*, Taylor & Francis.

[15] Iwama, K., Higuchi, K. and Maekawa, K., 2020. Thermo-mechanistic multi-scale modeling of structural concrete at high temperature, *Journal of Advanced Concrete Technology*, Volume 18, Issue 5, 2020; pp.272-293.

[16] Iwama, K. and Maekawa, K., 2022. Modeling of carbonation, de-carbonation and re-carbonation processes of structural concrete subjected to high temperature heating, *Cement and Concrete Composites*, Volume 129, 2022; Article ID: 104493.

[17] Iwama, K. and Maekawa, K., 2022. Redox

reaction models for carbonation of hardened cement under elevated temperature up to 1000°C, *Cement and Concrete Composites*, Volume 153, 2024; Article ID: 105738.

[18] Higuchi, K., Iwama, K. and Maekawa, K., 2021. Remaining shear capacity of fire-damaged high strength RC beams after moist curing, *Journal of Advanced Concrete Technology*, Volume 19, Issue 8, 2021; pp.897-912.

[19] Biot, M.A., 1963. Theory of stability and consolidation of a porous medium under initial stress, *Journal of Mathematics and Mechanics*, Volume 12, Issue 4, 1963; pp.521-541.

[20] Zažirej, S., Maekawa, K. and Hosoda, A., 2024. Poromechanical approach to blast-induced dynamic fracture in concrete, *Structural Concrete*, 2024; https://doi.org/10.1002/suco.202400551

[21] Picandet, V., Khelidj, A. and Bastian, G., 2001. Effect of axial compressive damage on gas permeability of ordinary and high-performance concrete, *Cement and Concrete Research*, Volume 31, Issue 11, 2001; pp.1525-1532.

[22] Gong, F. and Maekawa, K., 2019. Proposal of poro-mechanical coupling among ASR, corrosion and frost action for damage assessment of structural concrete with water, *Engineering Structures*, Volume 188, 2019; pp.418-429.

[23] Jean-Christophe Mindeguia, J.C., Pimienta, P., Noumowé, A. and Kanema, M., 2010. Temperature, pore pressure and mass variation of concrete subjected to high temperature -Experimental and numerical discussion on spalling risk, *Cement and Concrete Research*, Volume 40, Issue 3, 2010; pp.477-487.

[24] Felicetti, R., Monte, F.L. and Pimienta, P., 2017. A new test method to study the influence of pore pressure on fracture behaviour of concrete during heating, *Cement and Concrete Research*, Volume 94, 2017; pp.13-23.

[25] Kontani, O., Okayasu, T., Kawasumi, K., Ishikawa, S., Masaki, H., Tanaka, N., Goto, Y. and Ishioka, S., 2022. Effects of severe accident conditions on integrity of RPV pedestal of Fukushima Daiichi Nuclear Power Plant, Journal of Advanced Concrete Technology, Volume 20, Issue 7, 2022; pp.444-483.